

# Design, Modeling and Control of AVOCADO: A Multimodal Aerial-Tethered Robot for Tree Canopy Exploration

Steffen Kirchgeorg, Emanuele Aucone, Florian Wenk and Stefano Mintchev, *Member, IEEE*

**Abstract**—Forests provide vital resources and services for humanity, but preserving and restoring them is challenging due to the difficulty of obtaining actionable data, especially in inaccessible areas such as forest canopies. To address this, we follow the lead of arboreal animals that exploit multiple modes of locomotion. We combine aerial and tethered movements to enable AVOCADO to navigate within a tree canopy. Starting from the top of a tree, it can descend with the tether and maneuver around obstacles with thrusters. We extend our previous work with a new mechanical design with a protective shell, increased computational power and cameras for state estimation. We introduce a dynamic model and simulation, and perform a quasi-static and dynamic validation. For autonomy, we derive a control framework in simulation to regulate tether length, tilt and heading, before transfer to the robot. We evaluate the controllers for trajectory tracking through experiments. AVOCADO can follow trajectories around obstacles and reject disturbances on the tether. Exploiting multimodal mobility will advance the exploration of tree canopies to actively monitor the true value of our forests.

**Index Terms**—Aerial Systems; Mechanics and Control, Robotics in Agriculture and Forestry, Biologically-Inspired Robots, Multimodal Locomotion

## I. INTRODUCTION

Forests and their biodiversity enable human life on earth: they provide food and nutrients, act as a source of material and medicine, purify water and air as well as regulate our planet's climate. While the total economic value of these ecosystems may be as high as 16 trillion USD per year [1], species rich rainforests provide up to four times the monetary benefit (\$5264/ha/year) in ecosystem services compared to temperate (\$3013/ha/year) and low-density woodlands (\$1588/ha/year) [2]. Yet, these ecosystems continue to be lost at alarming rates. Agriculture, logging and livestock farming drive deforestation today, while a changing climate and invasive species will become major threats in the coming decades [3]. With our wealth and well-being depending on these ecosystems, it is vital that we learn how to protect and

Steffen Kirchgeorg, Emanuele Aucone and Stefano Mintchev are with the Environmental Robotics Laboratory, Dep. of Environmental Systems Science, ETH Zurich, 8092 Zurich, Switzerland and with the Swiss Federal Institute for Forest, Snow and Landscape Research (WSL), 8903 Birmensdorf, Switzerland (e-mail: skirchgeorg@ethz.ch, eaucone@ethz.ch, smintchev@ethz.ch). Florian Wenk is with the Institute of Environmental Engineering, Dep. of Civil, Environmental and Geomatic Engineering, ETH Zurich, 8092 Zurich, Switzerland and with the Swiss Federal Institute of Aquatic Science and Technology (EAWAG), 8600 Dübendorf, Switzerland (e-mail: fwenk@ethz.ch). This work was supported by the Swiss National Science Foundation through the Eccellenza Grant PCEFP2\_186865.



Fig. 1. Aerial-tethered robot AVOCADO deployed in a dense tree canopy.

conserve rainforests, while being able to sustainably exploit them for our demands.

However, a lack of data from within these environments makes these ecosystem services and their monetary benefit nearly invisible to us at a regional and local scale. As the "last biotic frontier", rainforests and their canopies remain incredibly hard to access and monitor [4].

Accessibility is the major challenge in acquiring in-situ data due to the high, dense, massively cluttered and dynamic nature of forest canopies, making it incredibly hard not only for humans, but also for robots to enter and move within them. Robotics research has mainly focused on two strategies to access these environments: i) contact-based terrestrial and climbing robots and ii) contact-free aerial robots. The former usually aims at first gaining access to the lower part of the tree and then adhering to the tree trunk and branches to locomote upwards into the canopy. Despite extensive development of climbing robots [5]–[7], it remains difficult to reliably perform complex maneuvers, such as moving from the tree trunk to smaller branches. Aerial robots, on the other hand, are already used for below- and above-canopy monitoring [8], [9], but flight below and especially within the canopy remains an ongoing research challenge. While micro drones have demonstrated flight below the canopy [10]–[12], their limited

flight time and payload reduce usefulness for environmental monitoring, whereas mechanical fragility limits operation in cluttered spaces. Dropping sensors from an unmanned aerial vehicle (UAV) [13] or shooting sensors from an aerial vehicle to the tree trunk like a dart [14] may allow placement of sensors without having to navigate within these environments, but it also limits the reach of these applications.

Contrary to our robotic approaches, arboreal animals are ideally adapted to their habitat and often capable of multiple means of locomotion. Wings allow birds to reach any place on earth, but their legs enable them to also walk, run, hop and even swim [15]. While not being able to fly, squirrels are extremely adapted to forests as they can locomote on nearly any surface in any orientation as well as leap and even glide from one branch to another [16]. On the other hand, spiders exploit their silk producing capabilities to extend their reach with spider webs. They can also move vertically with dragline silk or create a balloon to passively fly with the wind [17], [18]. All in all, nature hints us at exploiting multiple means of locomotion to move within diverse, dense and cluttered environments as forest canopies are.

Taking inspiration from arboreal animals' multimodal mobility, we presented a novel robot that exploits tethered and aerial locomotion to achieve the task of navigating through a tree canopy in our previous work [19]. The robot is anchored to the top of the canopy (Fig. 1) and uses a tether to descend or ascend, while propellers are used to navigate around obstacles. The tether makes the system (i) robust and safe as the tether can safely interact with the environment and secures the robot in case it collides with an obstacle. Therefore, collisions and destabilization does not mean immediate damage or crash of the platform. Furthermore, the tether allows (ii) low noise and power consumption during vertical movements and (iii) resting without noise and low power consumption below its last attachment point, which are both advantageous for environmental monitoring applications to increase mission time as well as reduce noise during monitoring. Finally, (iv) retrieval of the system is possible by spooling the tether even if thrusters fail or propellers get damaged. Complementing the tethered locomotion, aerial locomotion enables the robot to move in 3D space to overcome obstacles or move to certain areas within the canopy.

While small drones have increased maneuverability and mobility [10], [12], our platform is inherently safe with high energy efficiency for increased operating times and low noise for less invasive environmental monitoring. With respect to climbing robots, our locomotion strategy is more robust as it does not depend on adhesion and thus substrate properties.

In this article, we present the system design and dynamic modeling of the aerial-tethered robot AVOCADO as well as the implementation of a controller for onboard autonomy with validation in simulation and real world experiments. We elaborate on the initial contributions of our work on the aerial-tethered robot for tree canopy exploration presented at IROS 2022 [19] and extend it with the following contributions:

- 1) We revise the mechanical design by integrating a soft shell for protection, increased computational power and cameras for state estimation.
- 2) We derive a 3D dynamic model and simulation that take into account the tether length, and validate them, both in quasi-static and dynamic conditions.
- 3) We formalize a control strategy that decouples the tether length, pitch and heading control to enable the robot to autonomously follow 3D trajectories.
- 4) We validate the control strategy both in simulation and real-world experiments, characterize the response of the robot to perturbations on the tether, and subsequently demonstrate the ability of the robotic system to autonomously follow 3D trajectories, both indoors as well as outdoors in a cluttered tree canopy.

The rest of the article is organized as follows. Section II presents a review of tethered robots and drones and applied control frameworks. In section III, we introduce the locomotion strategy and design of AVOCADO. We formalize the dynamic model and simulation as well as validate them in section IV, and present the control strategy in section V. In section VI, we compare simulation data with experimental results and perform indoor and outdoor experiments with branch interaction and 3D trajectory following. Finally, we conclude with a focus on limitations and future challenges in section VII.

## II. RELATED WORK

Tethers are increasingly used in robotics for obvious benefits: increased stability and safety, reliable power transmission as well as high-bandwidth communication link. Within terrestrial robots, tethers have been exploited for nearly three decades mainly for locomotion, but also for navigation and planning tasks. Dante I and II [20], [21] used a tether to rappel into active volcanic craters and semi-autonomously locomote in this harsh environment. Already then, power, data and video telemetry were sent over the tether. More recent developments include NASA's Axel/DuAxel [22] and TRex [23]. DuAxel can rappel into extreme terrain by splitting into a mother-daughter system, with the mother serving as a save anchor point and power source for the daughter. Beyond locomotion, TRex uses tether information, i.e. tether length and bearing, for localization and mapping in cluttered environments to avoid tether entanglement.

In the field of aerial robotics, tethers are mainly being used for power and communication link [24], with 24/7-operable drones readily available on the market [25]. Other applications include cleaning and painting of buildings or firefighting, for which fluids can be brought to the flying platform through flexible hoses [26]. For these applications tethers may be slack, such that no tension acts along the link and only the weight and inertia of the tether or tube affects the robot. In this case, a standard position controller is sufficient to stabilize the UAV [27].

Drone applications with taut tethers include perching [28]–[30], take-off and landing on sloped terrain [31] or human interaction [32]. Contrary to slack tethers, an interaction force along the link arises for taut tethers, changing the dynamics of the aerial robot. This leads to non-optimal performance of standard flight-control methods or even makes them inappli-

cable due to the changed dynamics of the extended aerial-tethered system. For a drone on a taut tether, [33] estimates the drone pitch angle and tether angle with onboard inertial sensing only, and subsequently use this state estimation to stabilize and control the tethered drone in 2D. The work also shows the stabilization in 3D (except for yaw), with a bias in the tether angle estimation leading to a reduced stabilization performance.

While conventional cable-driven parallel robots (CDPRs) are being equipped with thrusters to improve payload capacity and enlarge the workspace [34], the concept of CDPRs is also transferred into aerial robotics for different use cases. To perform pick-and-place operations, a platform with a manipulator is suspended below multiple UAVs via cables, potentially reducing the need for heavy and costly infrastructure in construction [35]. Moreover, new aerial cable towed robots (ACTRs) are proposed that utilize land-fixed winches and taut tethers attached to UAVs to position the ACTR, i.e. an aerial platform, in a reconfigurable and adaptable workspace [36]. For instance, a platform equipped with water jets can be safely positioned close to high-rise buildings for firefighting.

Our aerial-tethered robot is different from existing tethered drones as we are simultaneously using the thruster and onboard tether actuation as two modes of locomotion. While steering the robot using the thrusters, we are spooling or unspooling the tether to extend the reach of the robot. Previous aerial robots exploiting tethers have a fixed tether length [28], [30]–[32], [35], slack tethers while unspooling [28], [29] and/or are not flying with the tether in tension [29]. Thruster-equipped CDPR and ACTR address interaction tasks with high load conditions, requiring a complex system with multiple robots and/or multiple tethers for stable operation [34], [36]. As AVOCADO's task is to navigate around obstacles in a tight environment, the system can be simplified to a single robot with one tether. Despite the theoretically extended workspace offered by CDPR and ACTR, our system may not benefit from multiple tethers due to the risk of entanglement and need to plan where to anchor them properly. Compared to other works, we also demonstrate our solution in a complex outdoor environment. Furthermore, our system distinguishes itself as it resembles an actuated pendulum with the robot suspended below an anchor point. Accordingly, this new locomotion and design concept requires new modeling and control approaches.

### III. LOCOMOTION STRATEGY AND MECHANICAL DESIGN

Our system is intended to be used together with a UAV for deployment as the top of forest canopies can easily be reached by aerial vehicles. While not part of this work, the deployment may be achieved directly from a drone or with an intermediate anchoring of our platform to a branch at the top of the canopy, as shown in Fig. 2A. After the deployment, AVOCADO subsequently enters the canopy and exploits two modes of locomotion, independently or simultaneously: tether-based and thruster-based locomotion. For the former, the robot uses its onboard tether and spooling mechanism to move vertically up and down with low power consumption and noise (Fig. 2C). As the tether is unspooled directly from the

robot, there is limited relative motion between the tether and environment. For the latter, the robot uses its two thrusters to generate forces to pitch from its vertical position (Fig. 2D) and change its heading (Fig. 2E). When combining tether (un)spooling, pitching and changing heading, 3D movements can be obtained as shown in Fig. 2F. By using each of these movements, AVOCADO can follow a 3D trajectory through the tree and navigate around obstacles, such as branches and leaves (Fig. 2A).

The workspace of the robot is an inverted cone starting from the anchor point with an opening angle of  $\theta$ , as also visible from Fig. 2F. The maximum workspace is defined by the maximum tether angle  $\theta_{max}$  of the system. This angle is either limited by the maximum thrust  $T_{max}$  or is bound by the maximum tilt thereafter the robot body flips around the tether attachment point (i.e. the rotary joint on the robot). The latter effect will be further discussed in section IV-E. The actual working space of the robot can be reduced from the maximum when the tether is constrained by obstacles.

The robot design is illustrated in Fig. 2B and main parameter definitions and characteristics are summarized in Table I. Compared to our previous work [19], we have reworked and improved the mechanical design of the platform. The new robot incorporates a soft, 3D printed shell (Varioshore TPU) that protects all internal components, including propellers, from damage in case of collision with obstacles. All components are attached to carbon-fibre profiles to create a stiff internal skeleton and avoid deformations due to thrust forces. Tether actuation is achieved with a continuous rotation servo (Dynamixel XL330-M288-T) connected to a 3D printed spool. The tether (SpiderWire,  $d = 0.39\text{ mm}$ ,  $F_{max} = 46\text{ kg}$ ) is routed via a wheel with an encoder (ams AS5047P) for tether speed estimation and through a rotary joint to the outside of the robot. The 3D printed rotary joint is equipped with a second rotary encoder (ams AS5047P) for an estimation of the inclination of the tether  $\varphi$ , which will be further explained in section IV. The heart of AVOCADO is a commercially available flight controller (FC) (HGLRC Zeus F722 Mini), electronic speed controller (ESC) (HGLRC Zeus 28A BLS) and a system on a chip (SoC) (Khadas VIM3). Two brushless DC motors (T-Motor F1507 3800KV) with 3 inch tri-blades (Gemfan 3052) can give an overall thrust of approximately 700 g. We have furthermore integrated a tracking camera (Intel RealSense T265) for state estimation.

### IV. DYNAMIC MODEL AND SIMULATION

Within this section, we first describe the dynamic model and define the equations of motion (EOM), before detailing the integration of the model in the simulation. We validate the model and simulation in quasi-static conditions as well as dynamically, and investigate a failure mode that determines static and dynamic limits of the system.

#### A. Model Description

The system is abstracted to a double pendulum, which consists of the robot body hanging on a mass-less tether (Fig. 3). We define three coordinate frames:  $\mathcal{I}$  (orthonormal basis  $\{\mathcal{I}x,$

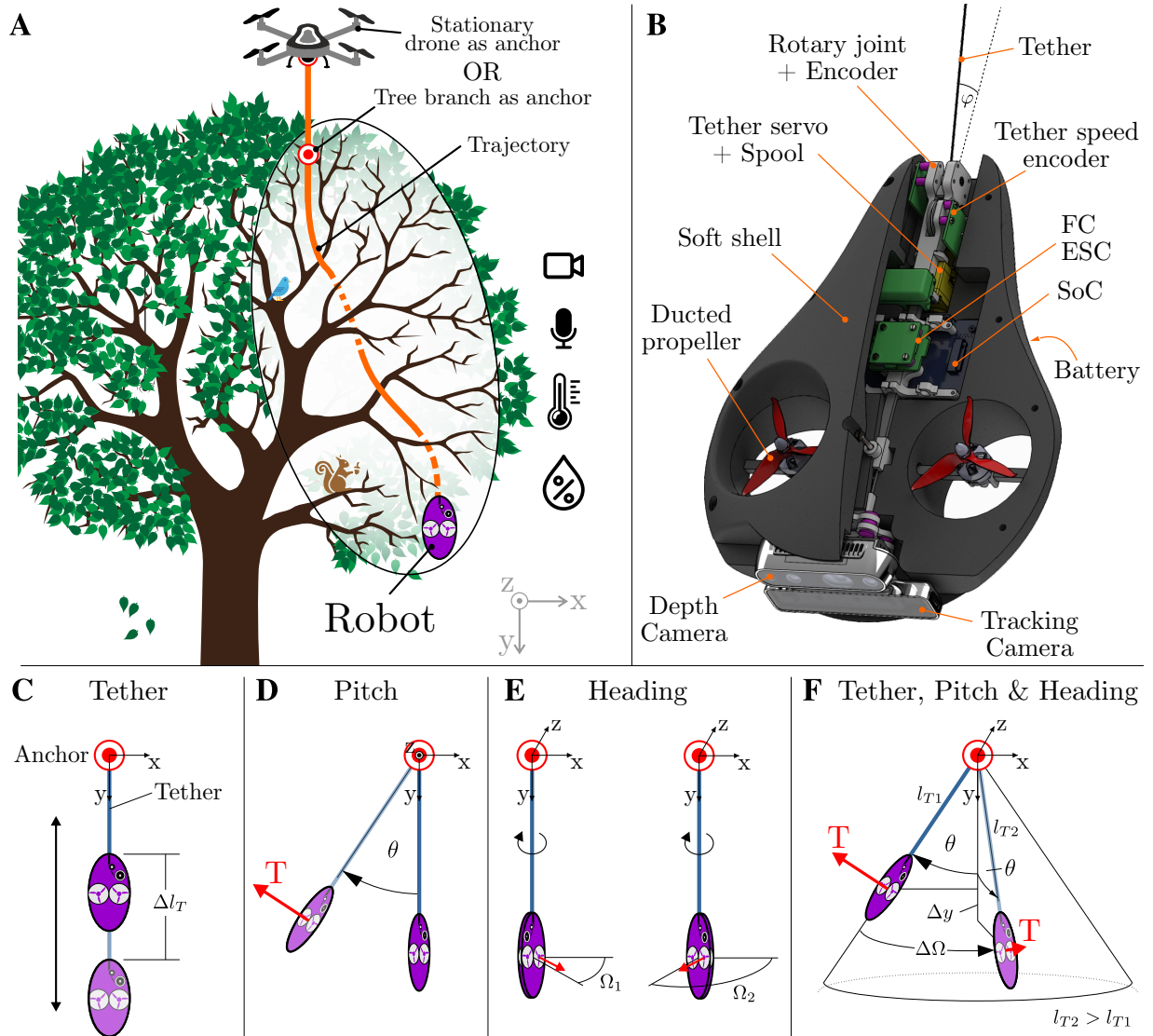


Fig. 2. Locomotion concept and design of AVOCADO: (A) Locomotion strategy of the aerial-tethered vehicle that enables 2D and 3D movement as well as resting. (B) Mechanical Design of the robot. (C)-(D) Locomotion Modes: (C) Vertical movement by unspooling or spooling the tether with the onboard tether servo, (D) pitching of the platform by increasing thrust, (E) change of heading by inducing a difference in thrust between the two thrusters. (F) Combination of the tether unspooling, pitching and changing heading enables 3D movements.

$\mathcal{I}y, \mathcal{I}z\}$  denotes the inertial, global frame which has the origin in the tether anchor O;  $\mathcal{P}$  (orthonormal basis  $\{p_x, p_y, p_z\}$ ) corresponds to a frame with center in the attachment between the tether and the robot (point P);  $\mathcal{F}$  (orthonormal basis  $\{f_x, f_y, f_z\}$ ) is the body frame, whose origin is in the center of gravity (COG) of the robot. Gravity is acting downwards (along  $\mathcal{I}y$ ) and the robot body is approximated as an elliptic plate.

The distance between point P and the COG is  $l_g$  and the distance between P and the location of applied thrust  $T$  (i.e. center of thrust (COT)) is  $l_{Th}$  along the axis  $p_y$  (Fig 3B). Each motor is placed at a distance  $l_{Th}^p$  perpendicular to the central axis  $f_y$  (Fig 3C) and the robot body is assumed symmetric about the  $y-z$  plane in the body frame  $\mathcal{F}$ .

The robot is initially considered as free-floating with the spherical coordinates  $[l, \theta, \Omega]$ .  $l$  is the direct distance between anchor O and point P of the robot. To add the tether constraint, we introduce the tether length  $l_T$  alongside a spring-damper

system to compute the tension acting on the robot along the tether direction:

$$F_T = \begin{cases} k_T(l - l_T) + d_T(\dot{l} - \dot{l}_T) & \forall l_T > l, \\ 0 & \forall l_T < l. \end{cases} \quad (1)$$

As no elongation or vibrations were observed during operation of the robot, high tether stiffness and damping coefficients of  $k_T = 10\,000 \text{ N m}^{-1}$  and  $d_T = 10\,000 \text{ N s m}^{-1}$  were used. In case the tether is in contact with an obstacle, as shown in Fig. 3D, the tether (and its length  $l_T$ ) wraps around branches while  $l$  remains the direct distance between O and point P. Therefore,  $l_T$  is adapted through geometric relations depending on the location of the obstacle and robot to properly compute the tension force  $F_T$  based on eq. (1). Additionally, we denote the distance between point P and the last interaction point of the tether with the environment (point B in Fig. 3D) with the free tether length  $l_f$ .



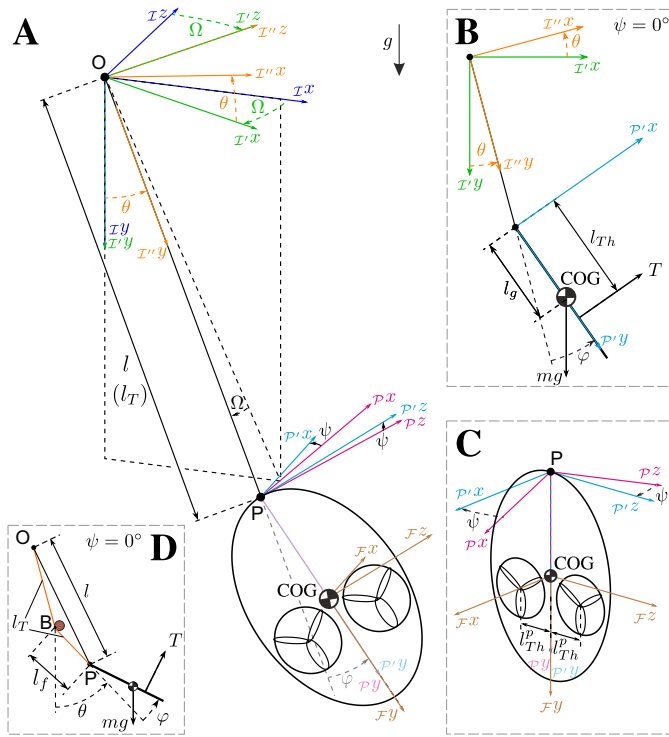


Fig. 3. Model and coordinate frame definitions (A) in 3D and (B) in 2D. (C) Vertical close-up of the model with roll  $\psi$ . (D) In case of contact with a branch B, the branch acts as a temporary anchor point, effectively reducing the tether length experienced by the robot from the total tether length  $l_T$  to the free tether length  $l_f$ . Note the difference between the tether length  $l_T$  and the coordinate  $l$  which are different in the case with an obstacle.

As the robot body has moments of inertia around the three body axes, the system acts as a double pendulum instead of a single pendulum, for which the body is usually assumed to be a point mass. It is worth to notice that standard double pendulum models consist of two point masses, whereas in our case the inertia of the rigid body has to be considered. We assume the inertia tensor  $\mathbf{J}$  to be a diagonal matrix with elements  $\mathcal{F}J_x$ ,  $\mathcal{F}J_y$ ,  $\mathcal{F}J_z$  because  $\mathcal{F}y$  and  $\mathcal{F}z$  are axes of symmetry, thus principal axes of inertia, and  $\mathcal{F}x$  has to be principal as it is orthogonal to the other two axes.

To introduce dissipation in the model, air resistance is considered as drag distributed over the robot body. Since the robot mostly works in a quasi-static condition with low velocity movements, the drag effect is generally low. Thus, instead of the usual quadratic drag  $\mathbf{F}_D = -1/2\rho c_A \mathbf{v}^2$ , we consider the linear drag to reduce model complexity:

$$\mathbf{F}_D = -c_D \int_A \mathbf{v} dA \quad (2)$$

where  $c_D = 1/2\rho c$  with  $c$  the drag coefficient of a flat plate and  $\mathbf{v}$  the velocity of each infinitesimal area  $dA$ . Furthermore, for the simulation results presented in section VI, numerical damping of  $\varphi$ ,  $\Omega$  and  $\psi$  was introduced to ensure numerical stability (Table I).

The thrust of each motor is assumed to act perpendicular to the robot plane  $\mathcal{F}y - \mathcal{F}z$  (Fig 3C). The thrust is transformed into virtual inputs:

$$T = T_l + T_r \quad (3)$$

$$\tau = (T_l - T_r) * l_{Th}^p \quad (4)$$

with  $T_l$  and  $T_r$  being the left and right motors' thrust respectively,  $T$  the collective thrust, and  $\tau$  the resulting moment around  $\mathcal{F}y$ . The torque generated by the propellers is neglected and we therefore do not consider a rotation around  $\mathcal{P}'x$ . Within our experiments (see section VI), we only observed small rotations that propagated to the tether and were dampened by it.

## B. Equations of Motion

The generalized coordinates  $\mathbf{q}$  and inputs  $\mathbf{u}$  are defined as:

$$\mathbf{q} = \begin{bmatrix} l \\ l_T \\ \Omega \\ \theta \\ \varphi \\ \psi \end{bmatrix} \quad \mathbf{u} = \begin{bmatrix} \dot{l}_T \\ T \\ \tau \end{bmatrix}. \quad (5)$$

with the angles definition shown in Fig. 3.  $\Omega$  is the heading angle (rotation around  $\mathcal{I}y$ ),  $\theta$  the tether angle (rotation around  $\mathcal{I}z$ ),  $\psi$  is the roll of the robot (rotation around  $\mathcal{P}y$ ),  $\varphi$  the tether-to-robot angle (rotation around  $\mathcal{P}'z$ ), and the sum  $\theta + \varphi$  is considered the robot pitch angle. As previously stated, we assume that no rotation around  $\mathcal{P}'x$  occurs, since damping in the system reduces oscillation in this direction. The assumption holds without loss of generality as the five generalized coordinates suffice to describe the controlled robot motion. The inputs  $\mathbf{u}$  include the tether velocity  $\dot{l}_T$  as well as the virtual inputs defined in eq. (3) and (4). The tether velocity  $\dot{l}_T$  is taken as input instead of the torque of the tether spooling servo as we can measure and control the speed of the servo motor on the robot, but not the motor torque itself.

With the given actuators, the system is underactuated and only three of the six degrees of freedom (DOF) can be controlled. Indeed, only the vertical position, the total robot pitch and the heading can be controlled, while the other three must be controlled with a combination of the previous. In terms of generalized coordinates, the length  $l_T$  and  $l$  are controlled through  $\dot{l}_T$ ;  $\psi$  is controlled through the torque  $\tau$ , resulting in a change in  $\Omega$ ; and the thrust  $T$  determines the total robot pitch ( $\theta + \varphi$ ), which in turn translates to its components  $\theta$  and  $\varphi$ . The rotation around  $\mathcal{P}'x$  is uncontrollable with the current actuators and assumed negligible in the simulation as such rotation would propagate to the tether and be dampened.

With this set of coordinates we employ the Euler-Lagrange equations,

$$\frac{d}{dt} \left( \frac{dL}{d\dot{\mathbf{q}}} \right) - \frac{dL}{d\mathbf{q}} = \mathbf{Q} \quad (6)$$

to derive the EOM with the Lagrangian  $L = E_k - E_p$  and the generalized forces  $\mathbf{Q}$ . To calculate the potential and kinetic energies,  $E_p$  and  $E_k$  respectively, and the generalized forces  $\mathbf{Q}$ , we calculate the positions and velocities of point P and the COG; then, the positions of the thrusters in the inertial frame  $\mathcal{I}$ , as well as the angular velocity  $\mathcal{F}\omega_R$  of the robot in the body frame  $\mathcal{F}$ . Noting that the robot body is the only object carrying a mass, this yields:

TABLE I  
SYSTEM PARAMETERS

Parameter	Symbol	Value	Unit
Robot Pitch Angle	$\theta + \varphi$	—	°
Tether Angle	$\theta$	—	°
Tether-to-Robot Angle	$\varphi$	—	°
Heading Angle	$\Omega$	—	°
Robot thrust	$T$	max. 7	N
Robot size		300x230x100	mm
Robot mass	$m$	0.74	kg
Robot inertia along $\mathcal{F}x$	$J_x$	$1.068 \cdot 10^{-3}$	$\text{kgm}^2$
Robot inertia along $\mathcal{F}y$	$J_y$	$3.991 \cdot 10^{-3}$	$\text{kgm}^2$
Robot inertia along $\mathcal{F}z$	$J_z$	$4.579 \cdot 10^{-3}$	$\text{kgm}^2$
Distance P - COG	$l_g$	0.154	m
Distance P - Thrust, along $\mathcal{F}y$	$l_{Th}$	0.19	m
Distance P - Thrust, along $\mathcal{F}z$	$l_{Th}^p$	0.06	m
Tether spring constant	$k_T$	10000	N/m
Tether damping constant	$d_T$	10000	$\text{Ns}^{-1}$
Aerodynamic drag coefficient	$c_D$	0.674	—
Ellipse half-axis along $\mathcal{F}y$	$a$	0.15	m
Ellipse half-axis along $\mathcal{F}z$	$b$	0.115	m
Numerical damping $\varphi$	$d_\varphi$	0.01	—
Numerical damping $\Omega$	$d_\Omega$	0.04	—
Numerical damping $\psi$	$d_\psi$	0.04	—
Simulation time step	$d_T$	0.01	s

$$E_p = -mg \mathcal{I}y_{\text{COG}} \quad (7)$$

$$E_k = \frac{1}{2} m \mathcal{I} \mathbf{v}_{\text{COG}}^T \mathcal{I} \mathbf{v}_{\text{COG}} + \frac{1}{2} \mathcal{F} \boldsymbol{\omega}_{\text{R}}^T \mathbf{J} \mathcal{F} \boldsymbol{\omega}_{\text{R}}, \quad (8)$$

where  $\mathcal{I}y_{\text{COG}}$  denotes the  $y$ -coordinate of the center of gravity and  $\mathcal{I} \mathbf{v}_{\text{COG}}$  the velocity of the COG in the inertial frame.

Computing the generalized forces is done by projecting them onto the velocity of the point of attack in the inertial frame  $\mathcal{I}$ . Taking an arbitrary force  $\mathbf{F}$  with point of attack  $p$ , this is written as

$$\mathbf{Q}_F = \frac{d \mathcal{I} \mathbf{v}_p}{d \mathbf{q}} \cdot \mathcal{I} \mathbf{F}. \quad (9)$$

Then, the generalized forces for each individual, non-conservative force are summed to obtain the total generalized force  $\mathbf{Q}$ . Note that for this robot, the drag is considered to be distributed over the plate. Therefore, each infinitesimal drag force is calculated and projected onto the points' velocity. Then, this generalized force density is integrated over the whole body.

Having calculated all the required components, the Lagrange equations (6) are evaluated and the equations of motion written in the classic form for robotic systems:

$$\mathbf{M}(\mathbf{q}) \cdot \ddot{\mathbf{q}} + \mathbf{b}(\mathbf{q}, \dot{\mathbf{q}}) + \mathbf{g}(\mathbf{q}) = \mathbf{Q}_d(\mathbf{q}, \dot{\mathbf{q}}) + \mathbf{Q}_i(\mathbf{q}, \dot{\mathbf{q}}, \mathbf{u}). \quad (10)$$

Hereby  $\mathbf{M}$  denotes the mass matrix,  $\mathbf{b}$  captures the inertial forces,  $\mathbf{g}$  the potential forces and the generalized forces are split into  $\mathbf{Q}_d$ , forces independent of the inputs and  $\mathbf{Q}_i$ , forces dependent on the inputs.

### C. Simulation Details

The dynamical model and the associated simulation is implemented in MATLAB (R2021b). In simulation, we use a time step of  $d_t = 0.01$  s (frequency equal to 100 Hz). Within

these timesteps, all inputs and references are kept constant, and MATLAB's ode15s function (a variable step, variable order method multi-step solver) is used to solve the dynamics (eq. 10). Motor dynamics associated with acceleration and deceleration are not modelled in the simulation, in which commanded thrust and torque are applied instantaneously at the desired time step.

We first generate the model based on the Euler-Lagrange equation (eq. (10)) before applying the given model constants (according to Table I). For simulations without active controllers, we set the initial conditions for  $\mathbf{q}$  and  $\mathbf{u}$ , as well as provide either constant or time-varying inputs (references)  $\mathbf{u}_{\text{ref}}$  to the system. For simulations with controllers, we instead initialize the controllers with the chosen parameters and set up a reference input, which is supplied to the controller at the desired time step. We then simulate the problem with the above mentioned solver. After the simulation, the results are plotted in an interactive window with an animation of the robot motion as well as plots of relevant variables. Detailed information on the controllers in simulation are summarized in Appendix A.

### D. Model and Simulation Validation

Robot specific system parameters were identified in Computer-Aided Design (CAD) or through measurements on the manufactured prototype. All system parameters used to compute the specific robot model are summarized in Table I. We first validated the model in quasi-static conditions before a dynamic validation, both for a tether length of  $l_T = 1$  m. We compare quasi-static simulation data against experimental data in Fig. 4A. For the experimental data (shaded lines), the thrust of the robot was slowly increased such that robot velocities were kept to a minimum. For simulation data (dashed lines), we calculated the state of the robot for a given thrust  $T$  by solving the EOM with velocities and accelerations set to zero. In Fig. 4A, the state of the robot, i.e. the angles  $\theta$ ,  $\varphi$ ,  $\theta + \varphi$ , are plotted over a mass-normalized thrust  $T/(mg)$ . The model data is matching well with experimental data with only slight deviations visible in maximum tether angle and mass-normalized thrust. As we could not directly measure the thrust of the platform during operation, the experimental data relies on a thrust mapping, which is likely the cause for the small offset in mass-normalized thrust.

As the thrust is increased, all angles experience a nearly linear increase before a sharp asymptotic behaviour. The tether angle  $\theta$  reaches a maximum before decreasing as  $\varphi$  rises asymptotically. Their sum, the robot pitch angle  $\theta + \varphi$  approaches  $90^\circ$  and the robot reaches a horizontal position. The horizontal force component of the thrust decreases, eventually leading to the tether collapsing towards a tether angle of  $\theta = 0^\circ$ . We have previously shown [19] that the limit of the thrust-to-mass ratio  $T_{\text{lim}}/(mg)$  equals the ratio  $l_g/l_{Th}$ , i.e. the ratio between location of COG to COT. While the validation case has a ratio  $l_g/l_{Th} < 1$ , with the actual limit being  $T_{\text{lim}}/(mg) = l_g/l_{Th} = 0.81$ , other robot configurations with  $l_g/l_{Th} = 1$  and  $l_g/l_{Th} > 1$  are possible. For further information on these configurations, we refer the reader to our

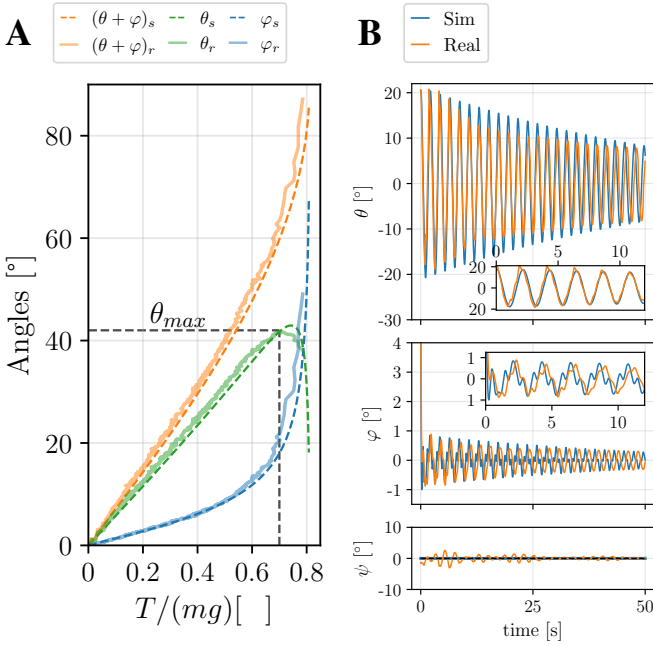


Fig. 4. Model and simulation validation with experimental data. (A) Quasi-static validation, i.e. negligible robot velocities, with the relationship of robot pitch angle  $(\theta + \varphi)$ , tether angle  $\theta$  and robot-to-tether angle  $\varphi$  over mass-normalized thrust  $T/(mg)$  at  $l_T = 1$  m. (B) Dynamic validation through swing motion. The experimental data was acquired by disarming the robot and leaving it swinging with no active control. The simulation uses the experimental data as initial conditions:  $l_T = 1$  m with  $\theta = 20.5^\circ$ ,  $\varphi = 4.8^\circ$ . High-frequency oscillations in  $\varphi$  were filtered for the simulation and experimental data to reveal underlying low-frequency oscillations. Insets show zoom-in of the initial seconds after disarming.

previous work [19]. It must further be noted that the steady state solution is independent of the heading and tether length, assuming negligible tether mass. The steady state solution only depends on the thrust-to-mass ratio and the mass distribution of the robot, as also shown in our previous work.

The dynamic validation experiment was carried out for a tether length of 1 m by applying a constant thrust to reach  $\approx \theta = 20^\circ$  before disarming the robot, such that it would swing back and forth without active control. The tether angle  $\theta$  and the tether-to-robot angle  $\varphi$  just before disarming were extracted from the experimental data and supplied to the simulation as initial conditions, i.e.  $\theta = 20.5^\circ$  and  $\varphi = 4.8^\circ$ . The experimental data along the simulation data is shown in Fig. 4B. In general, the experimental data aligns with the simulation data, while some differences can be observed. The frequency of the oscillations in  $\theta$  match well and only slightly shift towards  $t = 50$  s. The amplitudes in  $\theta$  match in the initial seconds, but diverge afterwards before converging again towards  $t = 50$  s. The faster decay is possibly due to the mismatch in aerodynamic drag and damping. As the simulation uses a simplified linear drag model compared to quadratic drag, the energy dissipation is underestimated at larger robot velocities. Besides drag, friction in the anchor point as well as in the tether joint on the robot are not modelled and can be the cause for additional damping in the real system. With respect to the tether-to-robot angle  $\varphi$ , both the simulation and experimental data were filtered to remove high-frequency oscillations and reveal the underlying low-frequency

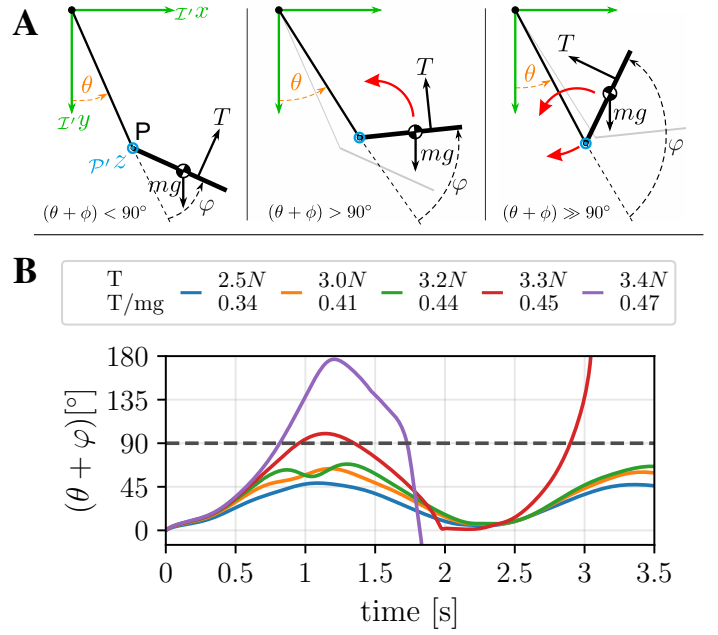


Fig. 5. (A) Failure mode of the robot as it exceeds the horizontal position, with subsequent collapse of the tether towards  $\theta = 0^\circ$  and for higher thrusts/accelerations a pronounced rotation around point P. (B) Dynamic simulations for which a constant thrust  $T$  was applied as a step at  $t = 0$  s. For large steps in thrust, the robot exceeds a total pitch angle  $(\theta + \varphi) = 90^\circ$ , i.e. a horizontal position, become unstable and ultimately the simulation crashes.

oscillations. Despite the values being very small in the range of  $-1^\circ$  to  $1^\circ$ , the data matches well in terms of amplitude and frequency. Overall, slight discrepancies can further arise from the rotation of the robot around its vertical axis  $\mathcal{P}'y$  ( $\psi$ ) during the experiment as it swings without any active control.

In summary, given both the quasi-static and dynamic validation, we have shown that our model and simulation capture the behavior of the robot well, allowing us to exploit the simulation as a tool to study the robot behavior and to safely develop controllers in simulation before transferring them to the robot.

### E. Static and Dynamic Limit

The robot enters a failure mode when the robot pitch angle  $(\theta + \varphi)$  exceeds  $90^\circ$ . This leads to a collapse of the tether, accompanied by a reduction of the tether angle, as well as a pronounced rotation (or even flip) of the robot around the tether attachment point P (around axis  $\mathcal{P}'z$  in Fig. 5A) on the robot.

In quasi-static conditions, the static validation in Fig. 4A shows the maximum tether angle  $\theta_{max}$ , beyond which the tether angle collapses towards  $0^\circ$ , with no steady state solutions beyond a total pitch angle of  $90^\circ$ . The maximum achievable tether angle for quasi-static operation is around  $42^\circ$  at a given  $T_{\theta, max}/(mg) \approx 0.7$ , resulting in a thrust of  $T_{\theta, max} \approx 4.9$  N. This can be considered a static limit of the robot. To avoid this condition, the thrust can be saturated to  $T_{\theta, max}$  in the controller.

In dynamic conditions, however, aggressive maneuvers could also cause the robot to enter this failure mode, as can be seen from dynamic simulations (Fig. 5B). By applying

a step in the thrust, a high acceleration causes the robot to exceed a total pitch angle of  $90^\circ$ . The greater the acceleration and velocities, the higher the likelihood of the robot flipping around point P, even before the tether collapses to  $\theta = 0^\circ$ . We investigated this behavior with five different thrusts ranging from 2.5 N to 3.4 N, or normalized thrusts of 0.34 to 0.47 respectively, in Fig. 5B. For normalized thrusts above 0.45 (i.e.  $T = 3.3$  N and  $T = 3.4$  N), the total pitch angle exceeds  $90^\circ$  and the simulation crashed within less than 3.5 seconds of simulation time, whereas for normalized thrusts up to 0.44 the robot eventually achieved a stable steady state. These steps in thrust can be translated into acceleration limits that should not be exceeded to ensure safe operation of the robot. For AVOCADO, the dynamic simulations show that accelerations of  $366^\circ/\text{s}^2$  and above for the total pitch angle lead to a failure of the system. It is particularly interesting how minor changes in the thrust and therefore acceleration lead to a large change in total pitch angle and subsequent failure.

To properly study the robot as well as develop controllers in simulation that violate a quasi-static operation (i.e. non-negligible accelerations and velocities), it is therefore essential to consider the static as well as dynamic behavior and limits of the system, which can be captured with the proposed dynamic model and simulation.

## V. CONTROL

For the application of navigating around obstacles (e.g. branches in a tree canopy), it is suitable to choose the tether attachment point P on the robot as the position to be controlled. When passing an obstacle, P denotes the highest point on the robot (with  $\theta + \varphi < 90^\circ$ ), allowing a quick assessment of whether the robot has passed the obstacle. After passing, contact of the tether with the obstacle can occur without robot collision. With this in mind, we decided to control point P of the robot in spherical coordinates by regulating the states: tether length  $l_T$ , tether angle  $\theta$  and heading angle  $\Omega$  as defined in Fig. 3.

In the following, we will describe the employed control approach and the developed controllers on the real robot as well as the state estimation.

### A. Control Approach

Three independent high-level controllers were incrementally employed in simulation and later implemented on the real robot: the first one is a planar controller to track the desired tether angle  $\theta$  (as depicted in Fig. 3B), the second controls the tether length  $l_T$ , and the last one regulates the heading angle  $\Omega$ . We separate the planar from the heading control as the planar coordinates  $\theta$  and  $\varphi$  only depend on the input thrust  $T$  and are independent of the heading  $\Omega$ . As visible from Fig. 6, neither the planar control nor the heading control depend on the length  $l_T$ , and vice versa. The tether length control is, indeed, directly related to the servo spooling velocity  $\dot{l}_T$ , which determines the length  $l_T$ .

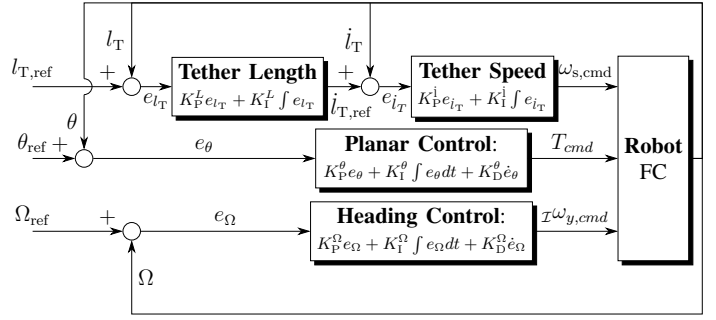


Fig. 6. An overview of the approach used to control the robot.

### B. Controllers on the Robot

The high-level controllers on the robot, shown in Fig. 6B, are implemented in the Robot Operating System (ROS) and, to achieve frequency matching between simulation and the robot, are running at 100 Hz. The robot inputs are the thrust  $T_{cmd}$  to control the tether angle  $\theta$ , the angular velocity  $\omega_{y,cmd}$  to control the heading  $\Omega$ , and the servo speed  $\omega_{s,cmd}$  to control the tether length. Regarding the latter, a rotary encoder (Fig. 2B) with a fixed diameter wheel is used to calculate the tether velocity, as the servo speed  $\omega_s$  cannot be accurately converted to a tether velocity  $\dot{l}_T$  due to a changing spooling radius. Therefore, a PI controller is added besides the tether length controller to compute the commanded servo speed  $\omega_{s,cmd}$ . The implementation of the controllers in simulation are detailed in appendix A.

### C. State Estimation

A tracking camera (Intel RealSense T265) is used to estimate the total pitch angle  $\theta + \varphi$  and the heading angle  $\Omega$ . At the rotary joint (Fig. 2B), a magnetic encoder is reading out the tether-to-robot angle  $\varphi$ , such that the tether angle  $\theta$  can be computed from the camera's total pitch angle. To estimate the tether length, the tether speed is integrated. The tether speed  $\dot{l}_T$  is measured by running the tether over a fixed radius wheel and reading out a magnetic encoder (Fig. 2B). Beyond orientation, the tracking camera uses visual-inertial odometry (VIO) to provide a position estimate in Cartesian coordinates in the camera world frame, which is used for visualization of the robot trajectory in section VI. The camera world frame, corresponding to our inertial frame  $\mathcal{I}$ , is initiated during startup of ROS and therefore depends on the camera's orientation during startup.

## VI. RESULTS AND DISCUSSION

In this section, we validate the controllers in simulation and through experiments on the real robot. First, we compare the simulation and experimental results for step responses of the planar controller and piece-wise linear references for the 3D control. Second, we investigate robot and controller behaviour in case of an abrupt change of tether length as well as disturbances to the anchor point. Obstacles may create intermediate anchor points, in which case the free tether length abruptly changes. Furthermore, these obstacles can oscillate and introduce disturbances to our robotic system. Finally,



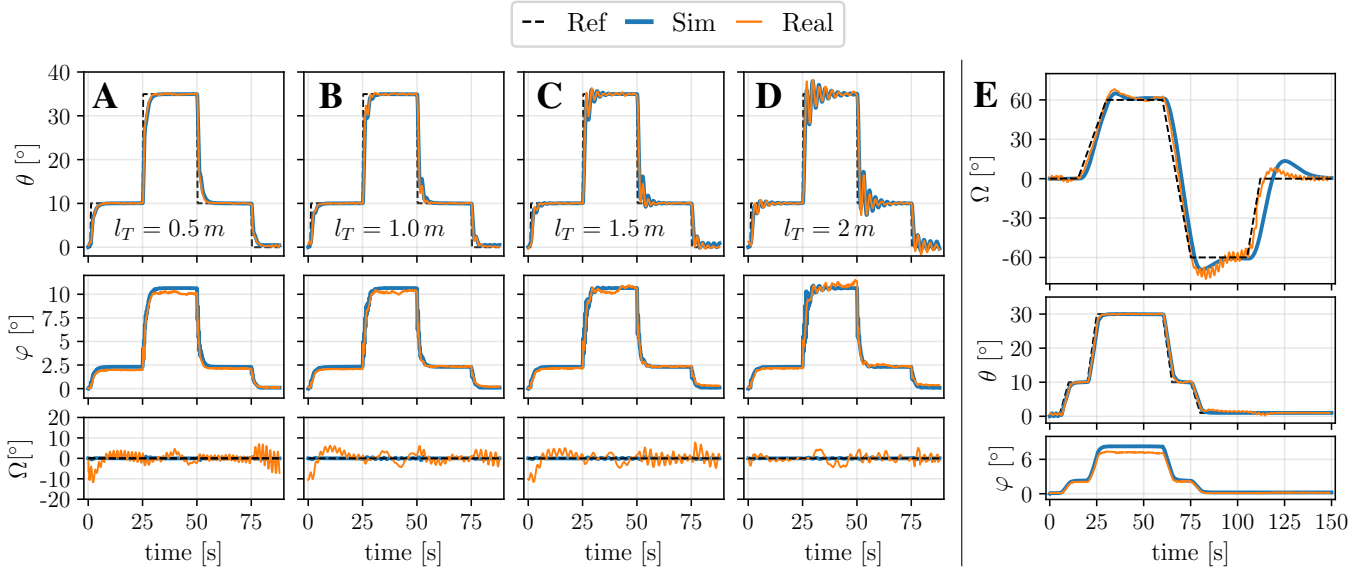


Fig. 7. Comparisons of controllers in simulation and on the robot for planar pitching (A-D) Responses of the PID controller at tether lengths of (A) 0.5 m, (B) 1 m, (C) 1.5 m and (D) 1.5 m for steps in  $\theta_{ref}$ . The reference heading angle  $\Omega$  was kept to  $0^\circ$ . (E) 3D control with piece-wise linear references on heading angle  $\Omega$  and tether angle  $\theta$  at a tether length  $l_T = 1$  m.

we showcase autonomous operation by following predefined trajectories around an artificial branch and hoop indoors as well as deploy AVOCADO outdoors in a tree.

#### A. Simulation vs. Experiment

We compare the behaviour of the system in simulation with experiments on the actual robot. The controllers have first been tuned in simulation at a tether length of 1 m before transfer to the real robot. The same gains were used for the planar controller in simulation and on the robot. The tether length and speed controller, as well as the heading and torque controller needed separate tuning.

We first investigate the system behaviour and control for different tether lengths, ranging from 0.5 m to 2 m. During operation in a cluttered tree canopy, branches will serve as intermediate anchor points (Fig. 3D) and effectively reduce the tether length, such that the robot is unlikely to experience free tether lengths beyond 2 m (see Fig. 8A and B). Step-references were given on the tether angle  $\theta$  and the step responses for  $\theta$ ,  $\varphi$  and  $\Omega$  are shown in Fig. 7A-C and the supplementary video S1. At low tether lengths (Fig. 7A), the robot has a very quick and smooth response. As the tether length increases, oscillations are observable in  $\theta$  around the step-reference but are quickly dampened by the system and the robot maintains the given reference with high accuracy. These oscillations can be attributed to an increase in inertia around the anchor point (O in Fig. 3) as the length increases. The simulation is nearly identical to the experimental data and also captures the above mentioned effect. The robot does not fully reach  $\theta = 0^\circ$ , but rather oscillates at a low angle due to the arming of the flight controller resulting in a low thrust at all times. By adding this constraint to the simulation (see appendix A), we are also able to match this behaviour. Small oscillations of  $\pm 10^\circ$  remain for the heading  $\Omega$  during all tests. The oscillation frequency

increases and thus the swing time period  $T_p$  reduces for lower tether lengths due to the inherent pendulum dynamics that state  $T_p = 2\pi \sqrt{L/g}$ . With respect to accelerations, the maximum acceleration for the different lengths lies between  $240^\circ/s^2$  and  $297^\circ/s^2$  in simulation, such that a sufficient safety margin is left to the dynamic limit of  $366^\circ/s^2$  identified in section IV-E.

A 3D control sequence of the robot is shown in Fig. 7E alongside simulation data. A trajectory consisting of piece-wise linear references in  $\Omega$  and  $\theta$  was given at a fixed tether length of 1 m. The heading control is responsive and tracks the given reference well at tether angles  $\theta > 0^\circ$ . At tether angles close to  $0^\circ$ , the robot responds slower and oscillates while trying to reach the target heading. This happens because the thrust cannot be negative (i.e. reverse the propellers), nor be reduced below the minimum thrust  $T_{min}$  due to the FC arming. Thus, no pure torque ( $T = 0, \tau \neq 0$ ) can be applied with the system but the produced torque is accompanied by a minimum thrust. Furthermore, the torque is lower than the (theoretical) desired one required to change the heading, i.e. one propeller increases the thrust and the other one is fixed to the min value. The controller in simulation has a similar behaviour at  $\theta \gg 0^\circ$ , but is slower to reach the desired heading at  $\theta \approx 0^\circ$ .

Bidirectional thrusters and propellers would increase the tracking performance of  $\theta$  and  $\Omega$  at small tether angles. Reversing the thrust would allow the robot to precisely apply the required torque for changing the heading while ensuring zero thrust. Furthermore, reverse thrust could be used to dampen oscillations in  $\theta$  for a reference of  $\theta \approx 0^\circ$ .

#### B. Abrupt Tether Length Change and Anchor Disturbance

In this experiment, we investigate the behaviour of the robot during interaction of the tether with a branch. When operating the robot in the intended environment, the tether will inevitably come into contact with obstacles. As the tether contacts the

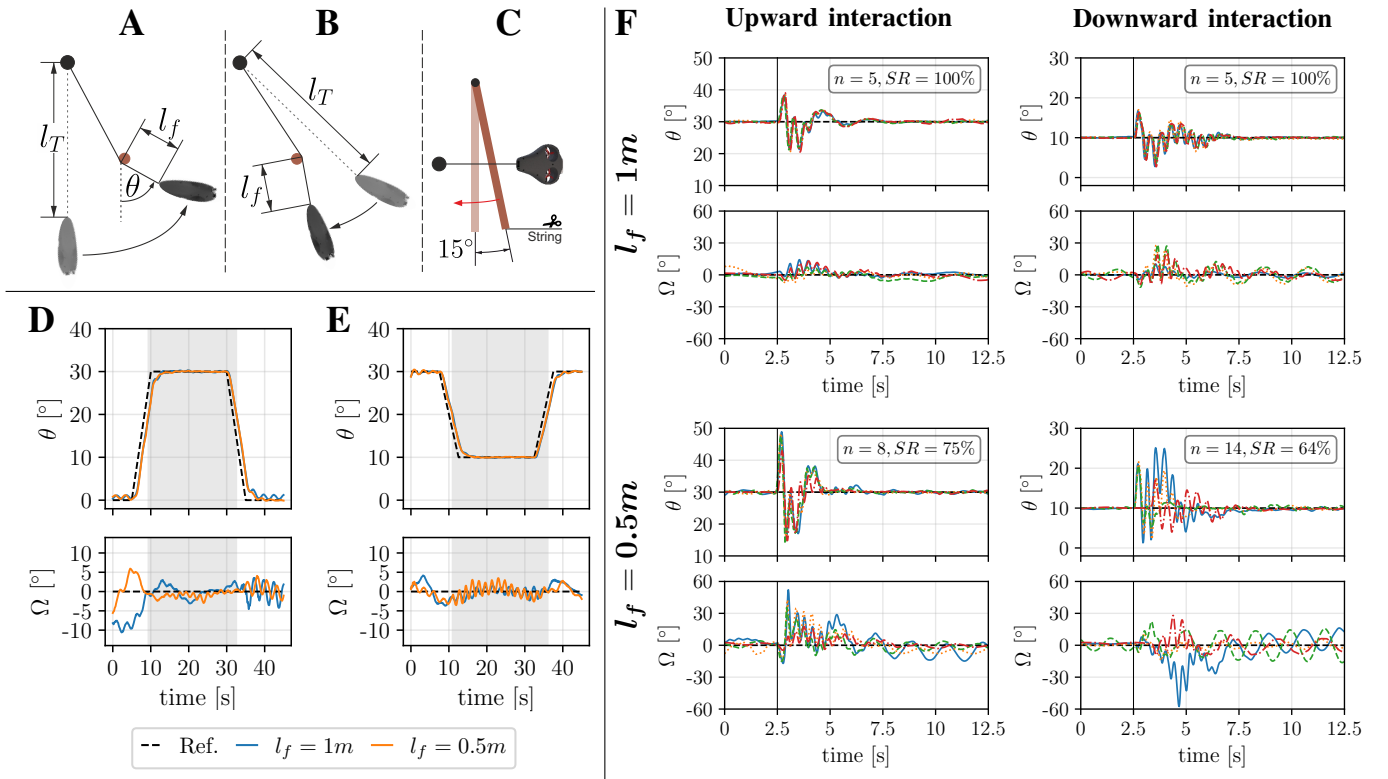


Fig. 8. Branch interaction and disturbance experiments. Experimental setup of (A) upward and (B) downward branch interaction with the tether length changing abruptly from total length  $l_T = 1.5$  m to the free tether length  $l_f = 1$  m and  $l_f = 0.5$  m. (C) Experimental setup of disturbance by deflecting the branch by  $15^\circ$  and releasing it abruptly. Results for (D) upward branch interaction, (E) downward branch interaction and (F) disturbance experiment for upward- and downward interaction for  $l_f = 1$  m and  $l_f = 0.5$  m with the disturbance introduced at  $t = 2.5$  seconds. Only successful attempts are shown with the given success rate (SR).

object, the object restricts the motion of the tether and acts as a new anchor point, from which the tether angle  $\theta$  is now defined (Fig. 3D, Fig. 8A/B). We define the free tether length  $l_f$  as the length of the tether from the robot to the last anchor point (Fig. 8A/B). Without obstacle interaction  $l_f$  is equal to  $l_T$ , whereas  $l_f < l_T$  during tether interaction with an obstacle. In this experiment, the free tether length  $l_f$  abruptly changes from  $l_f = l_T = 1.5$  m to  $l_f = 1$  m or  $l_f = 0.5$  m during interaction with an artificial branch made of a square aluminium profile. The branch's location was chosen such that the length changes were ensured. As rough tree bark limits sliding of the tether outdoors, we added thin foam to the metallic square profile to avoid sliding of the tether during the experiment. Due to compliance in the system, the branch could rotate  $\approx 15^\circ$  around its attachment point. Up- and downward interaction of the tether with the obstacle is shown in Fig. 8D and E. The shaded area shows the time at which the tether is in contact with the branch and the solid blue and orange lines denotes the states for free tether lengths of 1 m and 0.5 m. The control has no difficulties in coping with the changing free tether length as no significant oscillations in the states are visible.

To further test the system beyond nominal conditions, disturbances have been introduced by deflecting the branch and abruptly releasing it, as shown in the top view in Fig. 8C and in the supplementary video S2. The robot was brought to the nominal condition ( $\theta = 30^\circ$  and  $\theta = 10^\circ$  in Fig. 8A/B) with the branch deflected with a string by  $15^\circ$  and subsequently

released for the disturbance. This simulates a disturbance on the anchoring system, such as the tether sliding on the branch or swinging of the branch due to wind. For each free length, several attempts have been carried out with a plot of four successful attempts, the number of attempts  $n$  and the success rate (SR) shown in Fig. 8F. The disturbances result in a changing tether angle  $\theta$  and heading angle  $\Omega$ , which the robot has to dampen. In most cases, the controller is able to reject these disturbances. For the upward and downward interaction at  $l_f = 1$  m, the robot quickly dampens the oscillations and returns to its references. In case of the interaction with a shorter free tether length of  $l_f = 0.5$  m, we noticed that the robot is more susceptible to the disturbances. The success rate drops from 100% to 75% and 64% for upward and downward interaction with the short tether length. While the disturbances at the branch have been of the same magnitude, a long free tether length dampens the disturbance and the robot perceives a smaller disturbance. For the short tether length, the robot experiences a higher disturbance and struggles to dampen the oscillations in some cases, such that the robot becomes unstable.

### C. Autonomous Indoor and Outdoor Demonstration

In order to validate all three controllers in a relevant environment, we first performed an indoor demonstration before deploying AVOCADO outdoors. The robot was tasked with following trajectories defined through the state references  $\Omega$ ,

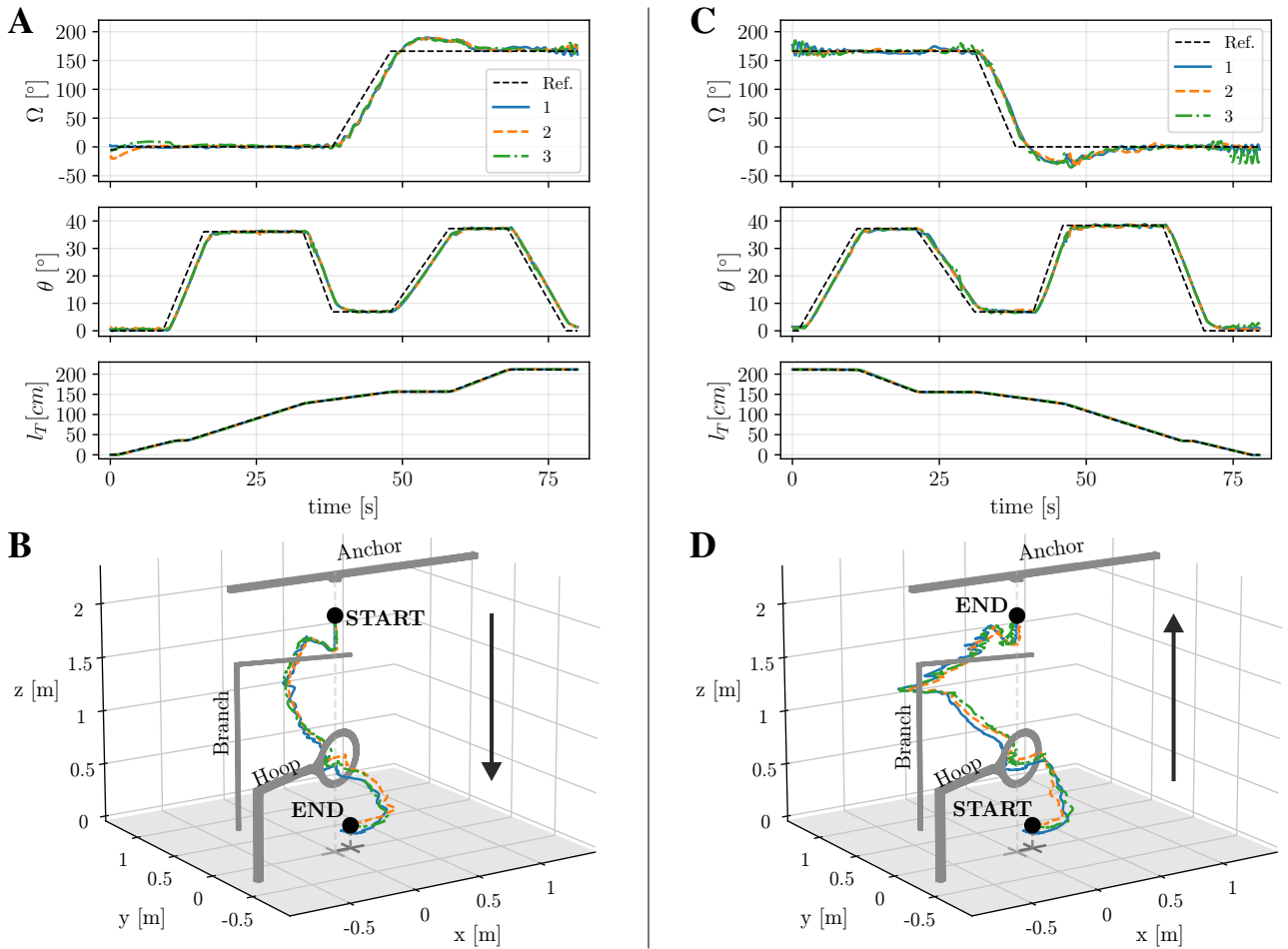


Fig. 9. Following of an indoor trajectory over a branch and through a hoop obstacle downward (A-B) and upward (C-D). (A,C) Desired and actual robot heading, tether angle and length and (B,D) 3D visualization of the recorded robot trajectory from the Intel RealSense T265 in Cartesian coordinates (x,y,z).

$\theta$  and  $l_T$ . The trajectories have been predefined manually and handled by a ROS node for execution. Videos of the indoor and outdoor demonstration can be found in the supplementary video S3.

For the indoor demonstration, the robot was suspended from a horizontal beam, and the scene included a horizontal branch (as described in section VI-B) and a hoop ( $d_{hoop} = 0.4$  m,  $d_{hoop}/w_{robot} = 1.75$ ). The robot had to pitch over the branch, change its heading by nearly  $180^\circ$  and pitch again to move through the hoop while continuously unspooling the tether, before reversing the motions to move back up to the starting position. The actual and reference states as well as the recorded 3D trajectory, taken from the tracking camera, are shown for three tests in Fig. 9, with downward trajectories shown in Fig. 9A/B and upward movements in Fig. 9C/D. For all three tests, the robot was able to follow the references and only a small overshoot was noticeable for the heading. No significant differences in the tether angle and length can be observed between downward and upward motion. However, the heading angle  $\Omega$  has some deviations, especially as the robot needs to pass back over the branch. The release of the tether from the branch together with the overshoot from the heading controller lead to a disturbance at  $t = 45$  s, which is also clearly visible in the 3D trajectories (Fig. 9D). Neverthe-

less, the robot is able to reject the disturbance, as previously shown in the branch interaction experiments (section VI-B), and continue its trajectory back to its starting position.

The recorded 3D trajectories (Fig. 9B/D) differ slightly as the robot had to be manually positioned correctly during code start-up, at which point the camera's world coordinate frames were initialized. Furthermore, a slight change in the tether contact point with the branch could result in a change in 3D trajectory due to the flexibility of the branch.

In terms of robot states, the platform is robust and reliable with no significant differences between tests (Fig. 9A/C). We computed the maximum and standard deviation of the state errors  $E$ , i.e.  $\max(|E|)$  and  $\sigma(|E|)$ , as well as the absolute tracking error  $E_a$  for all state variables  $x$  as:

$$E^k = x^k - x_{ref}^k, \quad (11)$$

$$E_a = \sqrt{\frac{1}{N} \sum_{k=1}^N (E^k)^2}, \quad (12)$$

with  $N$  the total number of recorded control cycles over the three tests. The results for the downward, upward and combined trajectory are summarized in Table II. In general, low errors are achieved for the three robot states, with the

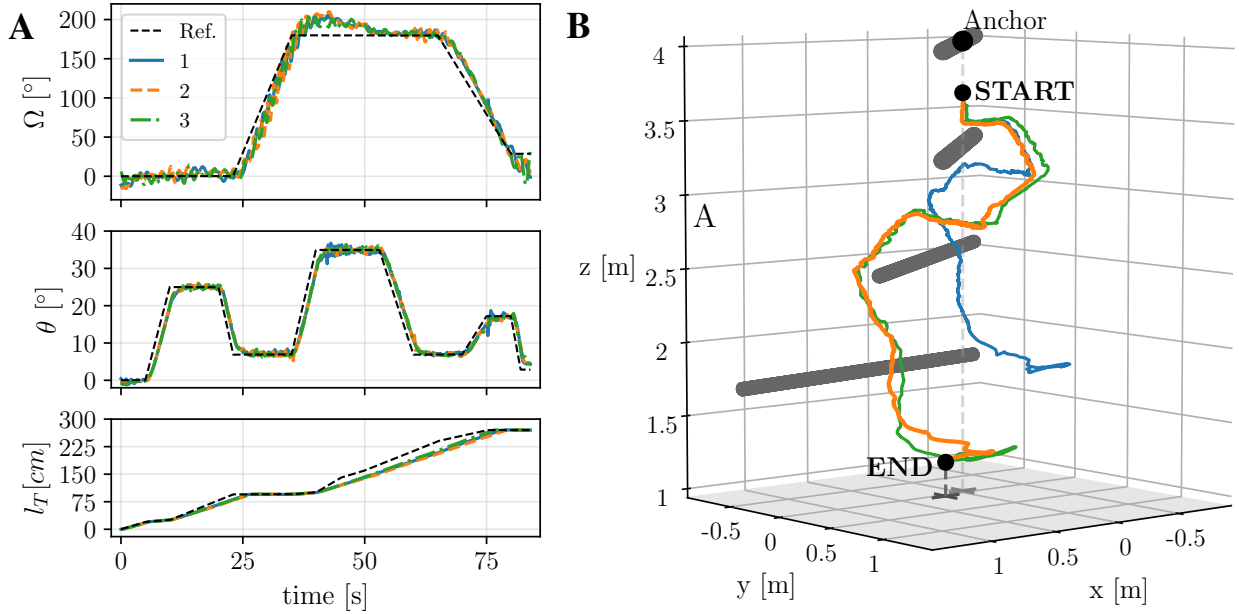


Fig. 10. Following of a predefined trajectory outdoor around multiple branches. (A) Desired and actual robot heading, tether angle and length. (B) 3D visualization of the robot trajectory in Cartesian space based on the tracking camera. Branch locations are purely qualitative and do not fully resemble the outdoor environment.

TABLE II

MAXIMUM AND STANDARD DEVIATION OF THE STATE ERROR  $E$  AND ABSOLUTE TRACKING ERROR  $E_a$  FOR THE THREE STATE VARIABLES  $\theta, \Omega$  AND  $l_T$  OVER THE CONTROL CYCLES OF THREE TESTS FOR THE INDOOR (DOWN, UP, COMBINED) AND OUTDOOR (DOWN) DEMONSTRATION.

Trajectory	Parameter	$\max( E )$	$\sigma( E )$	$E_a$	Unit
Indoor Down	$\theta$	6.61	2.06	2.88	deg
	$\Omega$	34.19	9.04	11.81	deg
	$l_T$	0.020	0.004	0.009	m
Indoor Up	$\theta$	7.60	2.14	3.06	deg
	$\Omega$	47.51	11.60	14.65	deg
	$l_T$	0.026	0.006	0.010	m
Indoor Combined	$\theta$	7.60	2.10	2.97	deg
	$\Omega$	47.51	10.42	13.30	deg
	$l_T$	0.026	0.005	0.010	m
Outdoor Down	$\theta$	6.60	1.83	2.49	deg
	$\Omega$	44.11	8.68	13.46	deg
	$l_T$	0.34	0.11	0.15	m

error in the heading angle  $\Omega$  being the largest, both in terms of the maximum error, mean and tracking error. The robot is able to better track the trajectory during the downward motion and a noticeable increase in error in  $\Omega$  can be observed for the upward motion due to the overshoot and tether release from the branch.

After ensuring repeatable and reliable indoor performance, we deployed the robot outdoors in a representative environment. The robot was manually attached to a tree branch roughly 4m above ground and followed a predefined trajectory around three branches downwards. The desired and actual robot states for three tests are shown alongside the 3D trajectory, obtained from the tracking camera, in Fig. 10. The robot was able to track the reference trajectory well with some oscillations visible for both the heading angle  $\Omega$  and tether

angle  $\theta$ . These disturbances are likely due to a combination of several factors: i) wind, ii) ground effects from surrounding branches and foliage, as well as iii) tether interaction with branches/foliage and slight slipping of the tether on the branches. In Table II, the maximum and standard deviation of the state errors  $E$  and the absolute tracking error  $E_a$  are listed for the outdoor demonstration. The tether angle and heading angle errors are comparable to the indoor downward demonstration. The error in the tether length  $l_T$  is larger due to the reference sent to the robot being too steep for the servo motor to match (Fig. 10A). Visualizing the position estimate in Cartesian space of the tracking camera (Fig. 10B) reveals that the position estimation drifted in one out of the three tests. While no ground truth is available, it is clear that the blue test shows significant position estimation drift after the first pitching motion at  $t \approx 20$  s, leading to a false estimated 3D trajectory for the remaining time. While forests provide a large amount of features for VIO, current depth and tracking cameras struggle to operate in these environments due to the low and constantly changing light conditions and dynamic movement of the environment. Our controller, working with the camera's orientation estimation, i.e.  $\Omega$  and  $\theta$ , was not affected by this drift in position and could complete the given task without a problem. Nevertheless, to further advance into a fully autonomous operation of the robot, accurate position estimation will be required to map the outdoor environment and for path planning algorithms to be successful.

## VII. CONCLUSION

In this work, we presented the aerial-tethered robot AVOCADO for locomotion in tree canopies in detail with respect to design, dynamic modeling and control. Taking our previous work as a basis, we improved upon our work with a

fully enclosed robot with a soft shell, increased computational power and the integration of a tracking camera for state estimation. We modeled the full dynamics of the robot, validated the model in quasi-static and dynamical conditions. We showed that static as well as dynamic limits need to be considered when simulating the robot behaviour. Therefore, we were able to transfer the controllers developed in simulation with some re-tuning of gains to the real robot with good results. Indoor and outdoor demonstrations showed that the robot is able to autonomously track a predefined trajectory around obstacles with high accuracy and precision. The developed controllers are robust to tether lengths of up to two metres, can handle tether interaction with obstacles and reject light disturbances due to wind and ground effects when operating inside the tree. Stronger disturbances can be rejected if the free tether length is sufficiently long. With respect to future works, the dynamic model also lays the foundation for investigating more advanced, model-based controllers. The main limitation is the need for human intervention for deployment. Currently, the robot needs to be manually deployed before operation. Furthermore, human intervention is needed in correctly orienting the robot during start-up as no global positioning nor orientation is available. While featuring a tracking and depth camera, this work does not cover the topics of visual perception and path planning in the target environment. Nonetheless, vision-based systems can contribute significantly by identifying gaps and optimal paths to safely navigate in traversable regions of the canopy. In fact, localization and mapping information could be utilized to estimate intermediate anchor points of the tether with the surrounding environment to possibly improve the control of the robot as well as to support path planning. Therefore, future work will investigate appropriate localization, mapping and path planning strategies, aiming to enhance autonomy in dense and cluttered settings. With a robot capable to autonomously operate within the tree canopy, novel data could be acquired to understand and actively monitor the true value of these ecosystems.

#### APPENDIX A CONTROLLER IN SIMULATION

We first developed the controllers in simulation (Fig. 11), moving incrementally from the 2D control of  $\theta$  and  $l_T$  to a full 3D control with  $\Omega$ . The high-level controllers were initially tuned in simulation, before implementation and further tuning on the hardware. Therefore, the high-level control architecture is identical with the robot. We provide references in the spherical coordinates  $l_T$ ,  $\theta$  and  $\Omega$  and in simulation compute the state based on the EOM, thus allowing us to compute the errors for the three controllers. The length controller is a P controller and outputs a commanded tether velocity  $\dot{l}_{T,cmd}$ . The planar controller is a PID controller with the output being a commanded thrust  $T_{cmd}$  to achieve the reference tether angle  $\theta_{ref}$ . The commanded thrust is saturated to a minimum thrust of  $T_{cmd} \geq 0.05$  N to replicate the hardware, in which arming the flight controller causes the propellers to spin at their minimum speed. The heading controller computes a reference angular velocity  $\omega_{y,ref}$  for the low level controller. The low

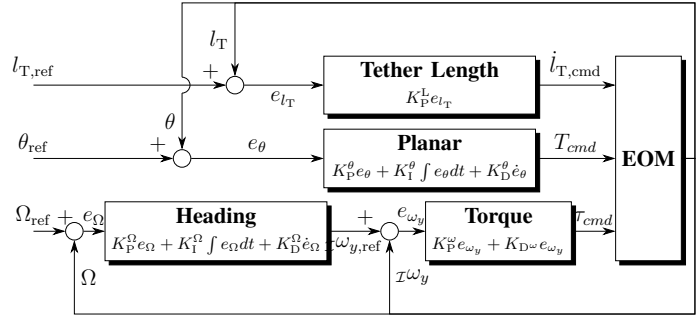


Fig. 11. An overview of the controllers used in simulation.

level torque controller then computes the input  $\tau_{cmd}$  to the robot model based on the error  $e_{\omega_y}$ .

An investigation on the FC hardware was required before implementing the low level torque controller adequately in simulation. The low-level controller feedback on the robot is based on gyroscopic data, which is measuring angular velocities with respect to the inertial frame axis ( $\mathcal{I}x$ ,  $\mathcal{I}y$ ,  $\mathcal{I}z$ ). As the angular velocity vectors  $\dot{\Omega}$  and  $\dot{\psi}$  are not orthogonal, they give rise to cross products when calculating the angular velocity  $\mathcal{I}\omega_y$  about the inertia's frame axes  $\mathcal{I}y$ . Therefore, the angular velocity  $\mathcal{I}\omega_y$  that the robot experiences and that needs to be controlled in simulation can be written as [37]:

$$\mathcal{I}\omega_y = \dot{\Omega} \cos(\theta) + \dot{\psi} \quad (\text{A.13})$$

according to the angle definitions in Fig. 3. This low-level controller on the robot is running at a rate of 4 kHz, whereas in simulation the main time step of  $d_T = 0.01$  s is used. Furthermore, in simulation the commanded torque  $\tau_{cmd}$  is directly applied, whereas on the robot the commanded torque is translated to a pulse-width modulation (PWM) signal for the motors by the FC.

#### REFERENCES

- [1] M. Rivers, A. C. Newton, S. Oldfield *et al.*, "Scientists' warning to humanity on tree extinctions," *Plants, People, Planet*, 2022.
- [2] R. de Groot, L. Brander, S. van der Ploeg *et al.*, "Global estimates of the value of ecosystems and their services in monetary units," *Ecosystem Services*, vol. 1, pp. 50–61, 2012.
- [3] BGCI, *State of the World's trees*. Botanic Gardens Conservation International, 2021.
- [4] T. L. Erwin, "Tropical forest canopies: The last biotic frontier," *Bulletin of the Entomological Society of America*, vol. 29, pp. 14–20, 1983.
- [5] G. Haynes, A. Khripin, G. Lynch *et al.*, "Rapid pole climbing with a quadrupedal robot," *2009 IEEE International Conference on Robotics and Automation*, pp. 2767–2772, 2009.
- [6] T. L. Lam and Y. Xu, "A flexible tree climbing robot: Treebot - design and implementation," *Proceedings - IEEE International Conference on Robotics and Automation*, pp. 5849–5854, 2011.
- [7] Q. Jiang and F. Xu, "Grasping claws of bionic climbing robot for rough wall surface: Modeling and analysis," *Applied Sciences*, vol. 8, p. 14, 2017.
- [8] C. Geckeler and S. Mintchev, "Bistable helical origami gripper for sensor placement on branches," *Advanced Intelligent Systems*, p. 2200087, 2022.
- [9] E. Aucone, S. Kirchgeorg, A. Valentini *et al.*, "Drone-assisted collection of environmental dna from tree branches for biodiversity monitoring," *Science robotics*, vol. 8, p. eadd5762, 2023.
- [10] A. Loquercio, E. Kaufmann, R. Ranftl *et al.*, "Learning high-speed flight in the wild," *Science Robotics*, vol. 6, p. 5810, 2021.
- [11] S. Kirchgeorg and S. Mintchev, "Hedgehog: Drone perching on tree branches with high-friction origami spines," *IEEE Robotics and Automation Letters*, vol. 7, pp. 602–609, 2022.



- [12] X. Zhou, X. Wen, Z. Wang *et al.*, "Swarm of micro flying robots in the wild," *Science Robotics*, vol. 7, 2022.
- [13] P. Pounds and S. Singh, "Samara: Biologically inspired self-deploying sensor networks," *IEEE Potentials*, vol. 34, pp. 10–14, 2015.
- [14] A. Farinha, R. Zufferey, P. Zheng *et al.*, "Unmanned aerial sensor placement for cluttered environments," *IEEE Robotics and Automation Letters*, vol. 5, pp. 6623–6630, 2020.
- [15] A. Abourachid and E. Höfling, "The legs: A key to bird evolutionary success," *Journal of Ornithology*, vol. 153, pp. 193–198, 2012.
- [16] N. H. Hunt, J. Jinn, L. F. Jacobs *et al.*, "Acrobatic squirrels learn to leap and land on tree branches without falling," *Science*, vol. 373, pp. 697–700, 2021.
- [17] M. Cho, P. Neubauer, C. Fahrenson *et al.*, "An observational study of ballooning in large spiders: Nanoscale multifibers enable large spiders' soaring flight," *PLOS Biology*, vol. 16, p. e2004405, 2018.
- [18] J. O. Wolff, "Locomotion and kinematics of arachnids," *Journal of Comparative Physiology A* 2021 207:2, vol. 207, pp. 99–103, 2021.
- [19] S. Kirchgeorg and S. Mintchev, "Multimodal aerial-tethered robot for tree canopy exploration," *2022 IEEE/RSJ International Conference on Intelligent Robots and Systems (IROS)*, pp. 6080–6086, 2022.
- [20] D. Wettergreen, C. Thorpe, and R. Whittaker, "Exploring mount erebus by walking robot," *Robotics and Autonomous Systems*, vol. 11, 1993.
- [21] J. E. Bares and D. S. Wettergreen, "Dante ii: Technical description, results, and lessons learned," *The International Journal of Robotics Research*, vol. 18, pp. 621–649, 1999.
- [22] I. A. Nesnas, J. B. Matthews, P. Abad-Manterola *et al.*, "Axel and duaxel rovers for the sustainable exploration of extreme terrains," *Journal of Field Robotics*, vol. 29, pp. 663–685, 2012.
- [23] P. McGarey, K. Mactavish, F. Pomerleau *et al.*, "The line leading the blind: Towards nonvisual localization and mapping for tethered mobile robots," *Proceedings - IEEE International Conference on Robotics and Automation*, vol. 2016-June, pp. 4799–4806, 2016.
- [24] F. Muttin, "Umbilical deployment modeling for tethered uav detecting oil pollution from ship," *Applied Ocean Research*, vol. 33, pp. 332–343, 2011.
- [25] "Fotokite." [Online]. Available: <https://fotokite.com/>
- [26] R. L. Dahlstrom, "State of technology: Cleaning and coating uav systems - industrial spray painting drones," *Proceedings of the Annual Offshore Technology Conference*, vol. 2020-May, 2020.
- [27] M. Tognon and A. Franchi, *Theory and Applications for Control of Aerial Robots in Physical Interaction Through Tethers*. Springer International Publishing, 2021, vol. 140.
- [28] K. Zhang, P. Chermprayong, T. M. Alhinai *et al.*, "Spidermav: Perching and stabilizing micro aerial vehicles with bio-inspired tensile anchoring systems," *2017 IEEE/RSJ International Conference on Intelligent Robots and Systems (IROS)*, pp. 6849–6854, 2017.
- [29] A. Braithwaite, T. Alhinai, M. Haas-Heger *et al.*, "Tensile web construction and perching with nano aerial vehicles," *Springer Proceedings in Advanced Robotics*, vol. 2, pp. 71–88, 2018.
- [30] H.-N. Nguyen, R. Siddall, B. Stephens *et al.*, "A passively adaptive microspine grapple for robust, controllable perching," *2019 2nd IEEE International Conference on Soft Robotics (RoboSoft)*, pp. 80–87, 2019.
- [31] M. Tognon, A. Testa, E. Rossi *et al.*, "Takeoff and landing on slopes via inclined hovering with a tethered aerial robot," *IEEE International Conference on Intelligent Robots and Systems*, vol. 2016-November, pp. 1702–1707, 2016.
- [32] M. Allenspach, Y. Vyas, M. Rubio *et al.*, "Human-state-aware controller for a tethered aerial robot guiding a human by physical interaction," *IEEE Robotics and Automation Letters*, vol. 7, pp. 2827–2834, 2022.
- [33] S. Lupashin and R. D'Andrea, "Stabilization of a flying vehicle on a taut tether using inertial sensing," *IEEE International Conference on Intelligent Robots and Systems*, pp. 2432–2438, 2013.
- [34] Y. Sun, Y. X. Guo, C. Song *et al.*, "Wrench-feasible workspace-based design of hybrid thruster and cable driven parallel robots," *Mechanism and Machine Theory*, vol. 172, p. 104758, 2022.
- [35] A. E. Jiménez-Cano, D. Sanalidro, M. Tognon *et al.*, "Precise cable-suspended pick-and-place with an aerial multi-robot system," *Journal of Intelligent & Robotic Systems*, vol. 105, 2022.
- [36] H. Jamshidifar and A. Khajepour, "Static workspace optimization of aerial cable towed robots with land-fixed winches," *IEEE Transactions on Robotics*, 2020.
- [37] W. T. Thomson, *Introduction to space dynamics*. Dover Publications, 1986.



**Steffen Kirchgeorg** received his Diploma in Mechanical Engineering and Aerospace from the Technical University of Dresden, Germany, in 2017.

He is currently a PhD Candidate at the Environmental Robotics Laboratory at ETH Zürich, Switzerland. His research focuses on multimodal robotic systems to achieve locomotion in cluttered environments. By combining different means of locomotion in novel designs, he is addressing environmental monitoring applications through the use of robotics in real-world scenarios. With his work, he aims to support larger scale monitoring to support nature conservation and restoration.



**Emanuele Aucone** received his B.Sc. Degree in Electronics Engineering for Automation and Telecommunication, from University of Sannio in 2017, and his M.Sc. Degree in Robotics and Automation Engineering, from University of Pisa, Italy in 2020.

He is currently a PhD Candidate at the Environmental Robotics Laboratory at ETH Zürich, Switzerland. His research interests are focused on design, perception and control of robotic systems operating within complex environments. He is currently investigating the development of aerial robots capable of physically interacting with flexible, natural environments for biodiversity monitoring within the forest ecosystem.



**Florian Wenk** received his M.Sc. degree in Robotics Systems and Control from ETH Zürich, Switzerland in 2022.

He is currently a PhD Candidate at the Institute of Environmental Engineering (IfU), D-BAUG, ETH Zurich, Switzerland and the Data & Information Group, Process Engineering Department at the Swiss Federal Institute of Aquatic Science and Technology EAWAG in Dübendorf, Switzerland. His research interests include modeling, model-based control and embedded applications. In his PhD he investigates

hybrid modeling, a modeling technique aiming to combine mechanistic and data-driven modeling techniques for the modeling of nitrous oxide emissions from wastewater treatment.



**Stefano Mintchev** (Member IEEE) received the B.S. and M.S. degree in mechanical engineering from the University of Pisa, Pisa, Italy in 2008 and 2010, respectively. He received the Ph.D. degree in biorobotics in 2014 from The BioRobotics Institute at the Sant'Anna School of Advanced Studies, Pisa, Italy.

Since 2020, he has been Assistant Professor of Environmental Robotics at ETH Zurich. His research interests include intersection between robotics and environmental science applied to nature conservation

and restoration. His primary goal is the development of versatile and robust robots capable of operating in complex natural environments. This research addresses scientific and technological questions on multi-modal mobility, perception and aerial physical interaction.